Imaging of red-shifted photons from bioluminescent tumours using fluorescence by unbound excitation from luminescence

FUEL imaging in tumours

Fabiane Sônego[1]*, Sophie Bouccara[1]*, Thomas Pons[2], Nicolas Lequeux[2], Anne Danckaert[1], Jean-Yves Tinevez[1], Israt S. Alam[1], Spencer L. Shorte[1] and Régis Tournebize[3]

*Contributed equally to this work.

1: UTechS Photonic BioImaging, Institut Pasteur, Paris, France

2: Laboratoire de Physique et d'Etude des Matériaux, ESPCI Paris, PSL Research University, CNRS UMR8213, Université Pierre et Marie Curie, Sorbonne-Universités, 10 rue Vauquelin, 75005 Paris, France

3: UTechS Photonic BioImaging, Unité Pathogénie Microbienne Moléculaire, INSERM U1202, Institut Pasteur, Paris, France

Current addresses: SB: Department of Neurobiology, Weizmann Institute of Science, Rehovot, Israel; FS: genOway, 181 Avenue Jean Jaurès, 69007 Lyon, France; ISA: Department of Radiology, Molecular Imaging Program at Stanford, Stanford University, Stanford, CA, 943065, USA.

Abstract

Early detection of tumours is today a major challenge and requires sensitive imaging methodologies coupled with new efficient probes. Bioluminescence imaging has been widely used in the field of oncology and several cancer cell lines have been genetically modified to provide bioluminescence signals. However, photons that are emitted by the majority of commonly used luciferases are usually in the blue part of the visible spectrum, where tissue absorption is still very high, making deep tissue imaging non-optimal and calling for optimised optical imaging methodologies. We have previously shown that red-shifting of bioluminescence signal by Fluorescence Unbound Excitation from Luminescence (FUEL) is a mean to increase bioluminescence signal sensitivity detection *in vivo*. Here, we applied FUEL to tumour detection in two different subcutaneous tumour models: the auto-luminescent human embryonic kidney (HEK293) cell line and the murine B16-F10 melanoma cell line previously transfected with the plasmid Luc2. Tumour size and bioluminescence were measured over time and tumour vascularization characterized. We then locally injected near infrared emitting Quantum Dots (NIR QDs)in the tumour site and observed a red-shifting of bioluminescence signal by (FUEL) indicating that FUEL could be used to allow deeper tumour detection.

43 **Introduction**

44

45 Imaging of physiological and pathological processes benefits from sensitive
46 methodologies [1] and new imaging probes and methodologies are constantly evolving
47 from the progress in preclinical research and important insights that it has yielded.
48 Preclinical and small-animal imaging modalities allow longitudinal and multiparametric
49 studies while reducing the number of animals used in the studies and thus comply with
50 ethical guidelines. They include MRI, SPECT, and PET [1, 2]. Whilst MRI and nuclear
51 imaging confer high resolution and sensitivity respectively, the cost of these scanners
52 and their maintenance represent major limitations in their use. By contrast, optical
53 imaging is a widely used and low-cost methodology, also offering high sensitivity but
54 also high throughput [3].
55 Bioluminescence imaging has been widely used in the field of oncology. Several cell lines
56 have been genetically modified to provide both *in vitro* and *in vivo* stable
57 bioluminescence signals. In most cases, tumour cells are modified to express the enzyme
58 luciferase and then a suitable substrate is added exogenously, which leads to the
59 production of light in presence of oxygen and ATP [3, 4]. Recently, autonomous
60 bioluminescent mammalian cell lines have been developed. These cell lines express both
61 codon-optimised *Photorhabdus luminescens* luciferases coding genes and associated
62 genes responsible for the production and recycling of aldehyde and $FMNH_2$ co-
63 substrates required for light emission. As a direct consequence, these cell lines do not
64 require substrate addition to be luminescent [5]. Photon production in bioluminescence
65 is chemically dependent, provides high sensitivity and low background signals, and
66 unlike fluorescence does not require external excitation sources. However, the optical
67 spectral region where luciferases maximally emit is between 480 and 620 nm, where

68 tissue absorption is maximum, highly limiting deep tissue bioluminescence imaging [6,
69 3] while a range of wavelengths between 650 and 900 nm is more suitable for *in vivo*
70 imaging [7]. Several strategies have been developed in the last few years to overcome
71 this limitation by red-shifting the emission in the well-adapted wavelength range where
72 tissue absorption is minimal. One of the strategies adopted is the Bioluminescence
73 Resonance Energy Transfer (BRET). BRET is a non-radiative process in which energy is
74 transferred from a bioluminescent donor to a fluorescent acceptor that has been shown
75 to be a powerful tool to evaluate protein-protein interaction [8, 9]. Based on the
76 principle of BRET, self-illuminated quantum dots (QDs) have been designed [10]. QDs
77 are inorganic fluorescent nanocrystals that are ideal candidate as BRET acceptor due to
78 their broad absorbance spectra, high absorbance cross sections, high fluorescence
79 quantum yield and their large Stokes shift in the near infrared (NIR) region [11]. In this
80 context, carboxylate QDs coupled with amide luciferase and even functionalized with a
81 RGD peptide have been developed for targeting *in vivo* cancer cells [12-14].
82 Recently, we reported Fluorescence by Unbound Excitation from Luminescence (FUEL)
83 as a mean to red-shift bioluminescence emission without requiring extremely close
84 contact between donor and acceptor like in BRET. FUEL is defined as a radiative transfer
85 between a bioluminescent source exciting nearby fluorophore [15, 16]. We have
86 hypothesized that FUEL could be a useful tool for the detection of tumours *in vivo* due to
87 two main advantages. Firstly, luciferase does not need to be grafted to the nanoparticles.
88 This would allow the use of smaller diameter nanoparticles, likely to have superior
89 pharmacokinetic properties in comparison to coupled larger nanoparticles [17, 18].
90 Secondly, because in FUEL, QDs red-emission is spatially correlated with the
91 bioluminescence emission of tumour cells, it is a relevant mean to increase the
92 sensitivity of the signal in tissue and is a marker of proximity.

In this study, we used two different *in vivo* subcutaneous bioluminescent tumour models to investigate the suitability of FUEL in detecting tumours. The first model was induced by bioluminescent B16-F10 tumour cells expressing firefly luciferase [19-21]. These cells will be referred here as B16-Luc2. The second tumour model established here was a bioluminescent HEK293 model, a human embryonic kidney cell line expressing the lux operon from bacteria and will hereon be referred as HEK-Lux. This cell type expresses both the luciferase and enzymes required for the production of the substrate, and therefore does not require further administration of substrate [5]. Using these two models, we present and quantify the first *in vivo* FUEL experiments using near-infrared emitting quantum dots to achieve a red-shifting emission of the subcutaneous tumours.

105 ***Methods***

106

107 Cell lines culture

108 The autobioluminescent HEK293 cells with the luxCDABE operon (HEK-Lux) cells were
109 kindly provided by 490 BioTech (Tennessee, USA)[22]. These cells were cultured at
110 37°C and 5% CO_2 in DMEM with Glutamax and Pyruvate (Life technologies)
111 supplemented with 10% heat-inactivated fetal bovine serum (FBS, Gibco), 1% of non-
112 essential amino acids (Sigma), 1% penicillin/streptomycin (Life technologies) and 100
113 µg/mL G418 (Sigma). The experiments were performed with cells at passage 20 to 22.
114 Non-autobioluminescent HEK293 cells were cultured in the same medium as HEK-Lux
115 cells, but in the absence of antibiotic G418. At confluence, cells were rinsed with
116 phosphate buffered saline without Ca^{2+} and Mg^{2+} (PBS, Gibco) and harvested with 0.05%
117 trypsin-EDTA (Gibco). Cells were used at passage 9.
118 The melanoma cell line B16-F10, expressing Luc2 (B16-Luc2) was kindly provided by
119 the group of Pierre Bruhns (Institut Pasteur, Paris). The cells were cultured in RPMI
120 1640 with glutamine and Hepes (Gibco) supplemented with 10% heat-inactivated FBS
121 and 1% penicillin/streptomycin. At maximum 50% of confluence, cells were rinsed with
122 PBS and harvested with 0.05% trypsin-EDTA. The experiments were performed with
123 cells at passages between 6 and 16.
124 The emission spectra of the HEK-Lux and B16-Luc2 cells were determined using $2x10^5$
125 cells suspended in 0.1 mL of appropriated medium. One day prior to imaging, cells were
126 seeded in a 96-well clear bottom black plate (Nunc) and incubated overnight at 37°C and
127 5% CO_2. The medium was gently removed from the wells and replaced with fresh
128 medium prior to image acquisition. For B16-Luc2 cells, the substrate D-luciferin (Perkin
129 Elmer) was added to the cells (150 µg/mL in 0.01 mL). Bioluminescence images were

130 acquired with an IVIS Spectrum system, using 20 nm bandpass emission filters and
131 OPEN mode (exposure time of 180 sec for HEK-Lux cells and 30 sec for B16-Luc2 cells).
132
133 Mice and ethics statement
134 Female nude mice (Rj:NMRI-nu) (7 weeks-old) were obtained from Janvier Laboratories
135 (France). All protocols involving animal experiments were approved and carried out in
136 accordance with the ethical guidelines of Institut Pasteur, Paris (license number: 2014-
137 0055). The mice were housed in the Biosafety Level 2+ animal facility of Institut Pasteur.
138 All mice had free access to food and water and were under controlled light/dark cycle,
139 temperature and humidity. Animals were handled with regard for alleviation of
140 suffering. Animals were anesthetized using isoflurane, and euthanized with CO2.
141
142 Induction of subcutaneous tumours
143 *HEK-Lux and non-bioluminescent HEK models:* Each tumour was induced by
144 subcutaneous (s.c.) administration of 0.1 mL of $5x10^6$ cells (suspended in medium
145 without FBS) and basement membrane matrix growth factor reduced (matrigel
146 Corning), (25:75, v/v).
147 *B16-Luc2 model:* Each tumour was induced by s.c. administration of 0.1 mL of $8x10^4$ cells
148 (suspended in medium without FBS) and basement membrane matrix growth factor
149 reduced (matrigel, Corning), (20:80, v/v).
150 For all cell lines, culture medium was replaced with fresh medium one day prior to the
151 subcutaneous injection.
152 Two ventral tumours were induced in each mouse. The mice were anesthetized with 2%
153 isoflurane gas prior to the injection of the tumour cells. Cells were first administered
154 subcutaneously on the left side and then on the right side of the mice. All the results

155 shown here represent measurements taken for the left tumour of each mouse. Tumour
156 growth was monitored by calliper measurement and determined as previously
157 described; volume = [(width/2)^2 x length] [23].
158
159 Near infra-red (NIR) QDs
160 NIR QDs were synthesized as previously described [24] and water-solubilized as
161 described in [25]. NIR QDs were diluted in PBS to provide the desired concentration.
162 Absorption and emission spectra of a 0.1 μM solution were determined using IVIS
163 Spectrum.
164
165 *In vivo* bioluminescence and fluorescence imaging
166 Bioluminescence and fluorescence imaging were performed using an IVIS Spectrum
167 system (Perkin Elmer). Unless specified elsewhere, mice bearing the
168 autobioluminescent HEK-Lux tumours were anesthetized with 2% isoflurane gas and
169 typically imaged with (840 nm) and without emission filter (total light output - open
170 filter) for 300 sec. Mice bearing the bioluminescent B16-Luc2 tumours were
171 intraperitoneally (i.p.) administered with the substrate D-luciferin (0.75 mg/mouse,
172 Perkin Elmer) 11 min prior to bioluminescence imaging. This time point was chosen to
173 allow a comparison between different mice and because it corresponds to the D-
174 luciferin peak bioavailability. Mice were anesthetized with 2% isoflurane gas
175 immediately after the administration of D-luciferin and maintained under anesthesia
176 until the end of the image acquisition. Bioluminescence images were acquired in the
177 open mode or with the 840 nm filter for 180, 60 or 3 sec, as specified in figures legends.
178 Fluorescence images were also acquired using IVIS Spectrum system (excitation filter

179 430 nm and emission filter 840 nm +/- 20 nm). Living Image software (Perkin Elmer)
180 was used to define and analyse the light emission in the regions of interest (ROIs).
181 *Angiosense 750EX:* The fluorescent vascular agent Angiosense 750EX (Perkin Elmer) was
182 administered intravenously (i.v.)(2 nmol/0.1 mL) in mice bearing HEK-Lux or B16-Luc2
183 tumours, 22 to 30 or 7 to 9 days post tumour cells injection, respectively. Mice were
184 anesthetized with 2% isoflurane gas prior to the image acquisition. The vascularization
185 of the tumours was evaluated 24 h post Angiosense 750EX administration using the IVIS
186 Spectrum system. Fluorescent images were acquired with 745 nm excitation filter and
187 800 nm emission filter, with the auto option selected as time of exposure.
188 *NIR QDs:* Fluorescent images using IVIS Spectrum were acquired prior and after NIR QDs
189 intratumoral administration *in vivo* with 0.1 sec of exposure time, and 430 and 840 nm
190 as excitation and emission filters, respectively.
191
192 Dextran- Fluorescein isothiocyanate (FITC)
193 High molecular weight dextran-FITC (500 KMW, Molecular Probes) was injected i.v. *via*
194 the retro-orbital sinus (0.5 mg/0.1 mL) in mice bearing HEK-Lux or B16-Luc2 tumours.
195 Harvested tumours were fixed in 4% parafolmadehyde (EMC) for 3 to 5 hours at room
196 temperature, depending on the tumour volume, followed by aldehydes quenching by 1 h
197 incubation in 100mM glycine (Sigma-Aldrich). Tumours were then incubated in 15%
198 sucrose (Sigma-Aldrich) at 4°C overnight and in 30% sucrose at 4°C for approximately
199 24 h before embedding in Shandon Cryomatrix (Thermo Fischer) and freezing using
200 isopentanol. Fifty µm sections cut using cryostat (CM3050 S, Leica) were stained with
201 DAPI and imaged using an automated spinning disk microscope CellVoyager1000
202 (Yokogawa Electrics, Japan). The sections were left overnight at room temperature
203 before being stained with DAPI.

204

205 FUEL experiments

206 *In vitro FUEL:* B16-Luc2, HEK-Lux and HEK non-bioluminescent cells ($2x10^5$, 0.1 mL of
207 appropriated medium) were seeded in a 96-well clear bottom black plate (Nunc) one
208 day prior to the experiment and incubated at 37°C and 5% CO_2. On the day of the
209 experiment, the medium was removed and a fresh medium with or without NIR QDs
210 (450 μM in 0.01 mL) was added to the well. Each cell type was cultured with the same
211 medium used for the cell culture. HEK non-bioluminescent cell type was used in this
212 experiment as a negative control for HEK-Lux cells. For B16-Luc2 cells, the substrate D-
213 luciferin was added to the wells (150 μg/mL in 0.01 mL), and the absence of the
214 substrate in the well was used as a negative control for this cell type. Bioluminescence
215 images were acquired with both 840 nm and open filter (exposure time of 300 sec for
216 HEK cells and 180 sec for B16-Luc2 cells). Fluorescence images were also acquired
217 (excitation 430 nm and emission 840 nm, 1 sec as exposure time).

218 *Experiments with mice bearing B16-Luc2 tumours:* In order to evaluate the
219 bioluminescence signal emitted at 840 nm before the administration of NIR QDs, D-
220 luciferin (0.75 mg/mouse, i.p.) was administered in mice bearing B16-Luc2 tumours 11
221 min prior to the image acquisition (180 sec as exposure time). After 1 h, bioluminescent
222 images were acquired again to determine the basal bioluminescent signal at 840 nm.
223 Next, 0.5 nmol (0.04 mL) NIR QDs were administered into the left tumour and 0.04 mL
224 PBS into the right tumour. Fluorescence images were acquired (excitation 430 nm/
225 emission 840 nm, 0.1 sec) prior and post NIR QDs intratumoral administration. D-
226 luciferin was then administered 11 min prior to the bioluminescence imaging
227 acquisition with a 840 nm and open filter for 180 and 3 sec, respectively.

228 Experiments were also performed to evaluate the possible effect of NIR QDs without a
229 bioluminescence source. For this control, NIR QDs were injected in the left tumour and
230 PBS was injected in the right tumour of the mice, without previous administration of D-
231 luciferin. Both bioluminescence and fluorescence images were acquired, using the same
232 emission and excitation filters and exposure time.
233 *Experiments with mice bearing HEK-Lux tumours:* Bioluminescence images at 840 nm
234 and open filter (300 sec of exposure time) were acquired prior and post injection of 0.5
235 nmol (0.04 mL) of NIR QDs in the left tumour and 0.04 mL of PBS in the right tumour of
236 mice bearing the autobioluminescent HEK-Lux tumours. Fluorescence images were
237 acquired (excitation 430 nm and emission 840 nm, 0.1 sec) prior and post NIR QDs
238 intratumoral administration.
239
240 Statistics
241 The number experimental repeats and animals used for each experiment are noted in
242 the figure legends. When compared, B16-Luc2 and HEK-Lux tumours results were
243 analysed via Mann-Whitney test or Student's t-test after being assessed for normality of
244 sample distribution. For the statistical analyses, the results from *in vitro* experiments
245 were analysed after normalization by strictly standardized mean difference (SSMD) test
246 as previously described [26]. Statistical analyses and graphs plotting were performed
247 using Prism 6.0 (GraphPad Software Inc.©, USA). P-values of *$p<0.05$ and **$p<0.001$ were
248 used.
249
250

251 **Results**

252

253 **Characterisation of tumour models reveals marked differences in**
254 **bioluminescence emission and growth dynamics but shows similar**
255 **vascularization**

256 In order to investigate the ability of FUEL to enhance the detection of tumours *in vivo*,
257 we used two distinct bioluminescent preclinical subcutaneous tumour models in nude
258 mice: murine B16-Luc2 melanoma tumours previously described [21] and the human
259 HEK 293 tumor model, adapted from the model described by Ho *et al.* [23].

260 Firstly, we characterised the emission spectrum for each of the tumoral cell types and
261 observed an emission peak at 600 nm for B16-Luc2 (Fig 1A), while for HEK-Lux the peak
262 was at 500 nm (Fig 1B). It is noteworthy that the B16-Luc2 cells emit a stronger
263 bioluminescent signal when compared to an equal number of HEK-Lux cells. B16-Luc2
264 cells also showed higher *in vivo* proliferation than HEK-Lux cells. While 8 x 10^4 B16-Luc2
265 cells induced the formation of 400 mm^3 tumours in 14 days (Fig 1C), 5 x10^6 HEK-Lux
266 cells were necessary to induced similar tumour sizes in more than 30 days (Fig 1D).

267

268 **Fig. 1: Characterisation of emission spectra of B16-Luc2 and HEK-Lux cells and**
269 **tumour growth curves**. A) Emission spectrum of B16-Luc2 and B) HEK-Lux cells.
270 Bioluminescence images were acquired from 500 to 840 nm for 30 sec (B16-Luc2) or
271 180 sec (HEK-Lux). Results are expressed as total flux (photons/sec) in the ROI, n=3. C)
272 Tumour growth of B16-Luc2 (8x10^4, 0.1mL) and D) HEK-Lux (5x10^6) cells over time,
273 following subcutaneous injection in nude mice on the right and left sides. Results are
274 representative of 4 independent experiments and represent the left tumour volume ,
275 n=5. Data shown are means ± SEM.

276

277 We also acquired bioluminescence images of tumours over time, and observed that
278 similar to the growth in tumour volume, the bioluminescence signal intensity of B16-
279 Luc2 tumours was detectable as early as 3 days post-injection and increased over time
280 to reach approximately 10^8 photons emitted/sec per tumour on day 14 (Fig 2A and 2C).
281 In contrast, though HEK-Lux cells emitted a high bioluminescence signal immediately
282 after the subcutaneous injection, this signal disappeared on day 1. The signal stayed low
283 until day 29, when it started to increase again, reaching a maximum of 10^5 photons/sec
284 per tumour on day 38 (Fig 2B and 2D). Interestingly, the signal increase correlated with
285 the development of the tumour, as assessed by an increase in tumour volume,
286 suggesting that the cells had a latency time before growing and emitting higher
287 bioluminescence signal. Altogether, these observations show that the two tumour
288 models have markedly different growth curves and that the B16-Luc2 tumours emit
289 1000 times more light using an open filter for detection than the HEK-Lux.

290

291 **Fig. 2: Tumour bioluminescence signal evolution imaging over time.** A) B16-Luc2
292 cells ($8x10^4$, 0.1mL) were subcutaneously administered in nude mice. Mice were imaged
293 1 day prior and 1, 3, 6, 9 and 14 days post administration of B16-Luc2 cells, n=5. B) HEK-
294 Lux cells ($5x10^6$, 0.1mL) were subcutaneously adminstered in nude mice. Mice were
295 imaged 6 days prior and 0, 1, 3, 8, 15, 22, 29 and 38 days post administration of HEK-Lux
296 cells, n=6. C) Bioluminescence signal quantitation of B16-Luc2- and D) HEK-Lux-induced
297 tumours. Red rectangles in 2A and 2B show the ROI used for quantification. Results
298 express the total flux (photons/sec) in the ROI of the left tumour of the mice. These
299 results are representative of 4 independent experiments.

300

301

302 We additionally investigated the vascularization of both tumours using the vascular
303 agent Angiosense 750EX. Fluorescence images acquired 24 h post Angiosense
304 administration indicated similar accumulation of the probe in both B16-Luc2 and HEK-
305 Lux-induced tumours (Fig 3A and 3B). Mice not bearing tumours were used as control,
306 and did not show fluorescence signal in the upper abdomen. The fluorescence signal
307 observed in the lower abdomen, in both control and tumour-bearing mice, is likely
308 associated with the renal excretion of the probe. In order to investigate the
309 vascularization at microscopic levels, we have administrated high molecular weight
310 dextran labelled with FITC i.v. Corroborating the results *in vivo*, histological sections
311 suggest that the vascularization is similar in both tumour models (Fig 3C and 3D).

312

313 **Fig. 3: *In vivo* evaluation of tumour vascularisation.** A) B16-Luc2 cells ($8x10^4$,
314 0.1mL), HEK-Lux (5×10^6, 0.1 mL) were subcutaneously administered in nude mice.
315 Angiosense 750EX (2 nmol, 0.1 mL) was intravenously administered between 7 and 9
316 days after B16-Luc2 injection or between 22 and 30 days post HEK-Lux cells injection
317 Images were acquired 24 hrs after. B) Fluorescence signal quantitation of Angiosense
318 accumulation in B16-Luc2- and HEK-Lux-induced tumours. ROIs were determined as
319 shown in the first image of Figure 3A. Results express the difference between the
320 average radiant efficiency in the ROI of the left tumour of the mice with tumour and the
321 arithmetic mean of the average radiant efficiency in the ROI of the left side in mice
322 without tumour, (n=4 control group and n=5 for the tumour bearing groups). C)
323 Vizualisation of tumour vascularization using high molecular weight dextran-FITC (500
324 KMW). Images correspond to a section in the tumors at 50% depth. Contrast and
325 brightness in both channels have been adjusted with an identical color scale across the

326 four images. Scale bars: 100 μm. D) Area of vascularisation, defined as the percentage of
327 the tumour area labelled by dextran at 0, 25, 50, 75 and 100% tumour depth. The area of
328 vascularisation was extracted using an identical threshold over all images.
329
330 **FUEL enables enhanced detection of tumours**
331 FUEL efficiency depends on the overlap between the emission spectrum of the
332 bioluminescent source and the excitation spectrum of the acceptor fluorophore. NIR QDs
333 have a broad and continuous decreasing excitation spectrum from UV to 800 nm, as
334 illustrated in Fig 4. This spectrum suggests that both B16-Luc2 (with an emission peak
335 wavelength centred at around 600 nm) and HEK-Lux bioluminescence signal (with an
336 emission peak wavelength centred at around 500 nm) are suitable for the excitation of
337 NIR. Additionally, emission spectrum indicates a maximum emission at around 840 nm.
338 The photoluminescence quantum yield was estimated at 20-30% using ICG in DMSO as a
339 standard fluorophore. Based on these spectra, we first investigated the presence of FUEL
340 with both B16-Luc2 and HEK-Lux *in vitro*. The incubation of B16-Luc2 cells with NIR
341 QDs significantly increased the bioluminescence signal at 840 nm as compared to cells
342 alone, and B16-Luc2 incubated with NIR QDs but in the absence D-luciferin (Fig 4B).
343 Normalized SSMD values classified the FUEL phenomenon extremely strong as
344 compared to the controls (Fig 4C). HEK-Lux cells, which emit weaker bioluminescence
345 signals, also showed an increase in the intensity of bioluminescence at 840 nm in the
346 presence of NIR QDs. The statistical analyses using SSMD normalization indicate a very
347 strong difference between HEK-Lux cells incubated with NIR QDs and controls (HEK-Lux
348 cells alone, and non-bioluminescent HEK cells incubated with NIR QDs) (Fig 4D). It is
349 important to mention that the scales for B16-Luc2 and HEK-Lux are different due to the

350 intensity of the bioluminescence emitted by each cell types. The presence of NIR QDs in
351 the specified wells was confirmed by the fluorescence images (Fig 4B).
352
353 **Fig. 4: *In vitro* investigation of FUEL with NIR QDs.** A) Excitation and emission
354 fluorescence spectra of NIR QDs. Results are expressed as total flux (photons/sec) B)
355 Bioluminescence (840 nm, exposure time of 60 sec (B16-Luc 2 cells) and 180 sec (HEK-
356 Lux cells), as well as fluorescence images (excitation 430 nm, emission 840 nm and
357 exposure time of 1 sec). C) Quantitation of bioluminescence signal emitted at 840 nm.
358 Results are expressed as normalized SSMD values for B16-Luc2 cells (B16-Luc2 cells +
359 D-luciferin used as control) or D) HEK-Lux (or non-bioluminescent HEK used as
360 control). n=8 (except for HEK-Lux + QD – n=6).
361
362 We next investigated the ability of FUEL to red-shift tumour emission at the NIR QDs
363 wavelength, enhancing the detection of tumour at red range wavelengths. Mice bearing
364 B16-Luc2 tumours were imaged after the i.p. administration of D-luciferin to evaluate
365 the background signal at 840 nm (-QD/+luciferin) (Fig 5A). After the intratumoral
366 injection of NIR QDs (+QDs/+luciferin), we observed a drastic increase in the
367 bioluminescence signal at 840 nm, confirming the presence of FUEL and its ability to
368 enhance tumour detection at 840 nm by red shifting the light emission. Fluorescence
369 imaging confirmed the presence of NIR QDs in the tumour sites and bioluminescence
370 imaging in open filter shows that both right and left tumours were bioluminescent upon
371 the administration of D-luciferin. No signal was observed in the absence of the substrate
372 (-QD/-luciferin and +QD/-luciferin).
373

374 **Fig. 5: *In vivo* evaluation of FUEL**. Bioluminescence imaging at 840 nm of B16-Luc2 (A)
375 or HEK-Lux (B) tumours prior (left image) or after quantum dots injection in the right
376 tumour (2nd image left). Fluorescence images and bioluminescence in open mode are
377 shown on the right. 840 nm bioluminescene images of control without luciferase for
378 B16-Luc2 Cells (A) or non bioluminescent HEK cells (B) are shown in the second row.
379 C) Quantitation of FUEL phenomenon. ROIs were determined as shown in the image of
380 Figure 5A. Results express the delta between total flux (photons/sec) in the ROI of the
381 left tumour of the mice post NIR QDs injection and prior to the NIR QDs injection, n=3
382 (negative control groups), n=6 (B16-Luc2) and n=4 (HEK-Lux). $p<0.05$ was considered
383 as significant: *$p<0.05$ and **$p<0.001$.
384
385 FUEL efficiency was also investigated in HEK-Lux-induced tumour model.
386 Bioluminescence signal at 840 nm post-intratumoral administration of NIR QDs was
387 stronger than pre-injection (-QD/HEK-Lux vs +QD/HEK-Lux, Fig 5B and 5C). NIR QDs
388 administered into non-bioluminescent HEK293 tumours showed bioluminescence signal
389 statistically similar to HEK-Lux tumours with NIR QD.
390 In summary, we have shown that both tumour models undergo a red shifting in their
391 emission via FUEL, where the red-shifting emission strongly depends on the optical
392 emission properties of the tumours and the quantum yield of the near-infrared emitting
393 fluorescent probe.
394
395 **Discussion**
396
397 The development of new techniques for detecting tumours in an accurate and simple
398 way is vital to support the search for new therapies in oncology. In this study, we used

399 two different bioluminescent tumour models to demonstrate for the first time, that the
400 FUEL process can be used *in vivo* to red-shift bioluminescence tumour emission and
401 enhance the detection of tumours.
402 Herein, we established two murine models of tumours to investigate FUEL. One of the
403 models was xenogeneic and made use of human (HEK-Lux) cells, an autobioluminescent
404 cell type [5]. The second model was syngeneic, induced by B16-Luc2, a murine
405 melanoma cell type expressing the enzyme luciferase frequently used in preclinical
406 oncology [27]. While B16-Luc2 tumour growth and their bioluminescence signal showed
407 the same profile, HEK-Lux cells initially presented a high bioluminescence activity
408 immediately after the subcutaneous injection before showing a marked decrease of this
409 activity the following day. We believe that these cells needed to adapt to the new
410 environment before propagating and forming the solid tumour. After this latency period,
411 the tumours reached the maximal volume that corresponded with the second peak of
412 bioluminescence emission.
413 Each of the developed models has advantages and disadvantages with regard to FUEL
414 applications. HEK-Lux cells have the enormous advantage of being autobioluminescent
415 due to its constitutive expression of the bacterial lux operon thus enabling convenient
416 image acquisition without having to consider the biodistribution kinetics of exogenously
417 added substrate *in vitro* or *in vivo*[5] as for the B16-Luc2 cells [20]. This required
418 substrate injection is a limitation since the time between substrate injection and imaging
419 needs to be strictly controlled to achieve reproducibility in the data, mainly when
420 acquiring images using different emission filters before and after the injection of NIR
421 QDs. In addition, melanin production by the B16-Luc2 cells might be a concern for this
422 type of imaging. However, we observed that melanin expression becomes significant

423 only 2 weeks after subcutaneous injection, after we performed our experiments, and
424 that these cells are indeed suited for FUEL imaging (Fig. 5).
425 FUEL is a phenomenon that allows the red shifting of the light, enhancing the detection
426 of bioluminescent tumours because of the reduction of tissue absorption and scattering
427 of blue/green light. One of the requirements for effective FUEL is that the fluorophore
428 should have a large Stokes shift, determining the requirement of an ideal bioluminescent
429 emitting source at approximately 500 nm [15, 16]. In this context, the wavelength of the
430 maximal bioluminescence emission peak of HEK-Lux cells would be another advantage
431 over B16-Luc2 cells regarding FUEL. Indeed, HEK-Lux cells emit luminescence at a
432 maximum peak of 490 nm [5]. By contrast, B16-Luc2 cells have a maximum emission
433 peak at 600 nm. In our case, we were still able to observe FUEL with B16-Luc2 because
434 we used NIR QDs, which have a large absorption range. Furthermore, B16-Luc2 cells
435 showed much stronger bioluminescence signal intensity in comparison to HEK-Lux cells,
436 requiring shorter exposure times during imaging and overall higher FUEL efficiency. Our
437 results show that even if HEK-Lux cells have a more appropriate maximum emission
438 wavelength to excite NIR QDs than B16-Luc cells, due to their lower luminescence
439 intensity, the red-shifting emission is not optimal. Indeed, if we focus on the maximum
440 emission wavelength of both cell types, 500 nm and 600 nm for HEK-Lux cells and B16-
441 Luc2 cells respectively, NIR QDs absorb 4 times less at 600 nm than at 500 nm (Fig 4A).
442 However, the emission of B16-Luc2 cells is about 800 times higher at their maximum
443 emission wavelength compared to HEK-Lux emission at their maximum emission
444 wavelength (when the same number of cells are compared). Even at 500 nm, B16-Luc2
445 emission is 14 times higher than HEK-Lux cells, for the same number of cells (Fig 4B).
446 These results highlight the fact that FUEL efficiency is controlled by a combination of
447 both luminescence spectrum and intensity and acceptor absorbance properties. NIR QDs

448 have many advantages for FUEL applications; namely high excitation coefficient and
449 photoluminescence quantum yield. Moreover, this specific type of NIR QD has been
450 shown to provide a lower *in vivo* toxicity compared to classical NIR QDs mainly because
451 they are not composed of heavy metals [28]. In addition, FUEL efficiency also depends
452 on the imaging conditions. The emission filters used in this study have a 20 nm
453 bandwidth, which limits the imaging of the red-shifted emission photons. Using larger
454 emission filter bandwidth or long pass emission filter should significantly improve the
455 FUEL efficiency.
456 Our results suggest that FUEL can be used to enhance the detection of deeper and
457 metastatic tumours by red-shifting their emission. As an optical method, FUEL has the
458 significant advantage of requiring affordable imaging systems and facilities [3] that are
459 extremely valuable in preclinical research. However, the experimental conditions of
460 FUEL phenomenon for detecting tumours warrants some improvement and
461 characterization to be fully suitable for enhanced detection of deeper tumours *in vivo*.
462 Several factors mainly need to be taken into account: the biodistribution of the QDs
463 within the xenograft, considering the tumour heterogeneity, and the fact that the tumour
464 micro-environment could affect both luciferase enzymatic efficiency and fluorophore
465 quantum yield, and consequently overall FUEL efficiency. The enhanced permeability
466 retention (EPR) effect exhibiting by tumours as a result of leaky vasculature, could
467 favour the retention of nanoparticles [29]. An effective EPR effect is strongly dependent
468 on the size of the nanoparticles, their surface chemistry and the type of tumour. For
469 instance, the accumulation and distribution of micelles of various sizes was not
470 substantially affected by the size in a colon adenocarcinoma (C26) model, while size
471 prove to be important in a human pancreatic adenocarcinoma (BxPC3) [30]. Positively
472 charged nanoparticles have been shown to have shorter circulation half-life, but

473 enhanced internalisation due to their adsorptive interaction with the cell membrane.
474 Interestingly, Yuan *et al.* demonstrated the enhanced tumoral retention of zwitterionic
475 nanoparticles with switchable charge based on environmental stimulus [29, 31]. In our
476 study, the i.v. injection of NIR QDs 0.05 nmol in our models did not result in tumour
477 retention, suggesting the absence of the EPR effect under our experimental conditions
478 (Supplementary Figure 1). We have shown that both tumour models are similarly
479 vascularised, which allows us to suggest that, with some improvement in our
480 experimental conditions, NIR QDs could reach the tumours via i.v. administration. One
481 alternative would be the targeting of tumours by coupling the nanoparticles with
482 antibodies or peptides. RGD (Arg-Gly-Asp) is a triple-peptide motif that has affinity
483 binding to the integrin $\alpha_v\beta_3$, which is highly expressed in neovasculature and many
484 tumour lines [32] and nanoparticles coupled to RGD have been shown to target tumours
485 and improve their visualization [33]. Antibody-coupled nanoparticles have also been
486 used for specific targeting of the tumour in preclinical imaging. NIR QDs or iron oxides
487 nanoparticles coupled to anti-HER2 showed high specificity in targeting subcutaneous
488 ovarian and prostate xenografts [34]. The NIR QDs used here could also be conjugated to
489 antibodies and/or targeting peptides like RGD to ensure accumulation in tumours and
490 provide more suitable experimental conditions to detect metastasis and deep tumours.
491 In summary, we have shown the development of two different tumour models and FUEL
492 ability to red shifting their emission. With further improvements, this optical method
493 could offer an attractive alternative for detecting smaller and deeper tumours.
494

495 **Acknowledgments**

496 We would like to thank Marie-Anne Nicola, Pascal Roux, Audrey Salles (Imagopole),
497 Patricia Flamant (Platform of Histology), Mai Ban, Naoko Furusawa and Yasushi Nakano

498 (Konica Minolta) who shared their insight and technical expertise, Biliana Teodorova
499 and Pierre Bruhns for providing the B16-Luc cells and Dan Close (490 BioTech) for
500 providing the HEK-Lux cells. This study was supported by NEDO-Konica Minolta, and
501 has received funding from the French Government's Investissement d'Avenir
502 programs Laboratoire d'Excellence "Integrative Biology of Emerging Infectious
503 Diseases" (grant ANR-10-LABX-62-IBEID) and Infrastructure d'avenir en Biologie Santé
504 " France Life Imaging " (grant ANR-11-INBS-0006). ISA was partially funded by a
505 Winston Churchill Memorial Trust UK Travel Fellowship.
506
507
508 **Supporting information legends**
509
510 **S1 Fig. Absence of QD EPR effect. A)** Fluorescence quantification in tumours and
511 abdominal control regions. B) representative image of fluorescence 24hours post QDs
512 injection showing tumours and control ROI.
513

514 **References**

515 1. Wehrl HF, Wiehr S, Divine MR, Gatidis S, Gullberg GT, Maier FC et al. Preclinical and
516 Translational PET/MR Imaging. Journal of nuclear medicine : official publication, Society
517 of Nuclear Medicine. 2014;55(Supplement 2):11S-8S. doi:10.2967/jnumed.113.129221.
518 2. Bernsen MR, Vaissier PE, Van Holen R, Booij J, Beekman FJ, de Jong M. The role of
519 preclinical SPECT in oncological and neurological research in combination with either
520 CT or MRI. European journal of nuclear medicine and molecular imaging. 2014;41 Suppl
521 1:S36-49.
522 3. O'Farrell AC, Shnyder SD, Marston G, Coletta PL, Gill JH. Non-invasive molecular
523 imaging for preclinical cancer therapeutic development. British journal of
524 pharmacology. 2013;169(4):719-35. doi:10.1111/bph.12155.
525 4. Marques SM, Esteves da Silva JC. Firefly bioluminescence: a mechanistic approach of
526 luciferase catalyzed reactions. IUBMB life. 2009;61(1):6-17. doi:10.1002/iub.134.
527 5. Close DM, Patterson SS, Ripp S, Baek SJ, Sanseverino J, Sayler GS. Autonomous
528 bioluminescent expression of the bacterial luciferase gene cassette (lux) in a mammalian
529 cell line. PloS one. 2010;5(8):e12441. doi:10.1371/journal.pone.0012441.
530 6. Close DM, Xu T, Sayler GS, Ripp S. In vivo bioluminescent imaging (BLI): noninvasive
531 visualization and interrogation of biological processes in living animals. Sensors.
532 2011;11(1):180-206. doi:10.3390/s110100180.
533 7. Frangioni JV. In vivo near-infrared fluorescence imaging. Current opinion in chemical
534 biology. 2003;7(5):626-34.
535 8. Pfleger KD, Eidne KA. Illuminating insights into protein-protein interactions using
536 bioluminescence resonance energy transfer (BRET). Nature methods. 2006;3(3):165-74.
537 doi:10.1038/nmeth841.

538 9. Wu P, Brand L. Resonance energy transfer: methods and applications. Analytical
539 biochemistry. 1994;218(1):1-13.
540 10. Xiong L, Shuhendler AJ, Rao J. Self-luminescing BRET-FRET near-infrared dots for in
541 vivo lymph-node mapping and tumour imaging. Nature communications. 2012;3:1193.
542 doi:10.1038/ncomms2197.
543 11. Michalet X, Pinaud FF, Bentolila LA, Tsay JM, Doose S, Li JJ et al. Quantum dots for live
544 cells, in vivo imaging, and diagnostics. Science. 2005;307(5709):538-44.
545 doi:10.1126/science.1104274.
546 12. So MK, Xu C, Loening AM, Gambhir SS, Rao J. Self-illuminating quantum dot
547 conjugates for in vivo imaging. Nature biotechnology. 2006;24(3):339-43.
548 doi:10.1038/nbt1188.
549 13. Kamkaew A, Sun H, England CG, Cheng L, Liu Z, Cai W. Quantum dot-NanoLuc
550 bioluminescence resonance energy transfer enables tumor imaging and lymph node
551 mapping in vivo. Chemical communications. 2016;52(43):6997-7000.
552 doi:10.1039/c6cc02764d.
553 14. Yuan A, Hu Y, Ming X. Dendrimer Conjugates for Light-activated Delivery of
554 Antisense Oligonucleotides. RSC advances. 2015;5:35195-200.
555 doi:10.1039/C5RA04091D.
556 15. Dragavon J, Blazquez S, Rekiki A, Samson C, Theodorou I, Rogers KL et al. In vivo
557 excitation of nanoparticles using luminescent bacteria. Proceedings of the National
558 Academy of Sciences of the United States of America. 2012;109(23):8890-5.
559 doi:10.1073/pnas.1204516109.
560 16. Holland AD, Ruckerl F, Dragavon JM, Rekiki A, Tinevez JY, Tournebize R et al. In vitro
561 characterization of Fluorescence by Unbound Excitation from Luminescence:

562 broadening the scope of energy transfer. Methods. 2014;66(2):353-61.
563 doi:10.1016/j.ymeth.2013.09.005.
564 17. Perrault SD, Walkey C, Jennings T, Fischer HC, Chan WC. Mediating tumor targeting
565 efficiency of nanoparticles through design. Nano letters. 2009;9(5):1909-15.
566 doi:10.1021/nl900031y.
567 18. Choi HS, Liu W, Misra P, Tanaka E, Zimmer JP, Itty Ipe B et al. Renal clearance of
568 quantum dots. Nature biotechnology. 2007;25(10):1165-70. doi:10.1038/nbt1340.
569 19. Danciu C, Falamas A, Dehelean C, Soica C, Radeke H, Barbu-Tudoran L et al. A
570 characterization of four B16 murine melanoma cell sublines molecular fingerprint and
571 proliferation behavior. Cancer cell international. 2013;13:75. doi:10.1186/1475-2867-
572 13-75.
573 20. Albanesi M, Mancardi DA, Macdonald LE, Iannascoli B, Zitvogel L, Murphy AJ et al.
574 Cutting edge: FcgammaRIII (CD16) and FcgammaRI (CD64) are responsible for anti-
575 glycoprotein 75 monoclonal antibody TA99 therapy for experimental metastatic B16
576 melanoma. Journal of immunology. 2012;189(12):5513-7.
577 doi:10.4049/jimmunol.1201511.
578 21. Albanesi M, Mancardi DA, Jonsson F, Iannascoli B, Fiette L, Di Santo JP et al.
579 Neutrophils mediate antibody-induced antitumor effects in mice. Blood.
580 2013;122(18):3160-4. doi:10.1182/blood-2013-04-497446.
581 22. Xu T, Ripp S, Sayler GS, Close DM. Expression of a humanized viral 2A-mediated lux
582 operon efficiently generates autonomous bioluminescence in human cells. PloS one.
583 2014;9(5):e96347. doi:10.1371/journal.pone.0096347.
584 23. Ho DH, Vu H, Brown SA, Donohue PJ, Hanscom HN, Winkles JA. Soluble tumor
585 necrosis factor-like weak inducer of apoptosis overexpression in HEK293 cells promotes

586 tumor growth and angiogenesis in athymic nude mice. Cancer research.
587 2004;64(24):8968-72. doi:10.1158/0008-5472.CAN-04-1879.
588 24. Bouccara S, Fragola A, Giovanelli E, Sitbon G, Lequeux N, Pons T et al. Time-gated cell
589 imaging using long lifetime near-infrared-emitting quantum dots for autofluorescence
590 rejection. Journal of biomedical optics. 2014;19(5):051208.
591 doi:10.1117/1.JBO.19.5.051208.
592 25. Tasso M, Giovanelli E, Zala D, Bouccara S, Fragola A, Hanafi M et al. Sulfobetaine-
593 Vinylimidazole Block Copolymers: A Robust Quantum Dot Surface Chemistry Expanding
594 Bioimaging's Horizons. ACS nano. 2015;9(11):11479-89. doi:10.1021/acsnano.5b05705.
595 26. Mellouk N, Weiner A, Aulner N, Schmitt C, Elbaum M, Shorte SL et al. Shigella
596 subverts the host recycling compartment to rupture its vacuole. Cell host & microbe.
597 2014;16(4):517-30. doi:10.1016/j.chom.2014.09.005.
598 27. Overwijk WW, Restifo NP. B16 as a mouse model for human melanoma. Current
599 protocols in immunology. 2001;Chapter 20:Unit 20 1.
600 doi:10.1002/0471142735.im2001s39.
601 28. Pons T, Pic E, Lequeux N, Cassette E, Bezdetnaya L, Guillemin F et al. Cadmium-free
602 CuInS2/ZnS quantum dots for sentinel lymph node imaging with reduced toxicity. ACS
603 nano. 2010;4(5):2531-8. doi:10.1021/nn901421v.
604 29. Blanco E, Shen H, Ferrari M. Principles of nanoparticle design for overcoming
605 biological barriers to drug delivery. Nature biotechnology. 2015;33(9):941-51.
606 doi:10.1038/nbt.3330.
607 30. Cabral H, Matsumoto Y, Mizuno K, Chen Q, Murakami M, Kimura M et al.
608 Accumulation of sub-100 nm polymeric micelles in poorly permeable tumours depends
609 on size. Nature nanotechnology. 2011;6(12):815-23. doi:10.1038/nnano.2011.166.

610 31. Yuan YY, Mao CQ, Du XJ, Du JZ, Wang F, Wang J. Surface charge switchable
611 nanoparticles based on zwitterionic polymer for enhanced drug delivery to tumor.
612 Advanced materials. 2012;24(40):5476-80. doi:10.1002/adma.201202296.
613 32. Martelli C, Lo Dico A, Diceglie C, Lucignani G, Ottobrini L. Optical imaging probes in
614 oncology. Oncotarget. 2016;7(30):48753-87. doi:10.18632/oncotarget.9066.
615 33. Li C, Wang W, Wu Q, Ke S, Houston J, Sevick-Muraca E et al. Dual optical and nuclear
616 imaging in human melanoma xenografts using a single targeted imaging probe. Nuclear
617 medicine and biology. 2006;33(3):349-58. doi:10.1016/j.nucmedbio.2006.01.001.
618 34. Gao J, Chen K, Miao Z, Ren G, Chen X, Gambhir SS et al. Affibody-based nanoprobes
619 for HER2-expressing cell and tumor imaging. Biomaterials. 2011;32(8):2141-8.
620 doi:10.1016/j.biomaterials.2010.11.053.
621

Figure 1

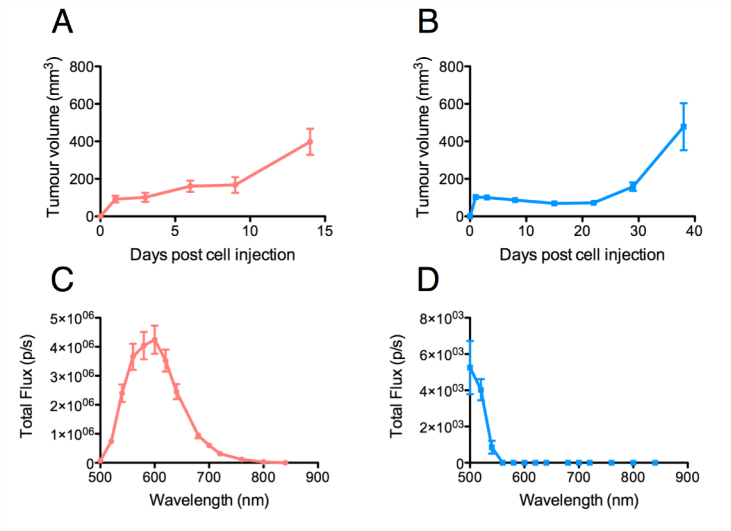
A
Tumour volume (mm3)
800
600
400
200
0
0
5
10
15
Days post cell injection
B
Tumour volume (mm3)
800
600
400
200
0
0
10
20
30
40
Days post cell injection
C
Total Flux (p/s)
5×10^06
4×10^06
3×10^06
2×10^06
1×10^06
0
500
600
700
800
900
Wavelength (nm)
D
Total Flux (p/s)
8×10^03
6×10^03
4×10^03
2×10^03
0
500
600
700
800
900
Wavelength (nm)

Figure 2

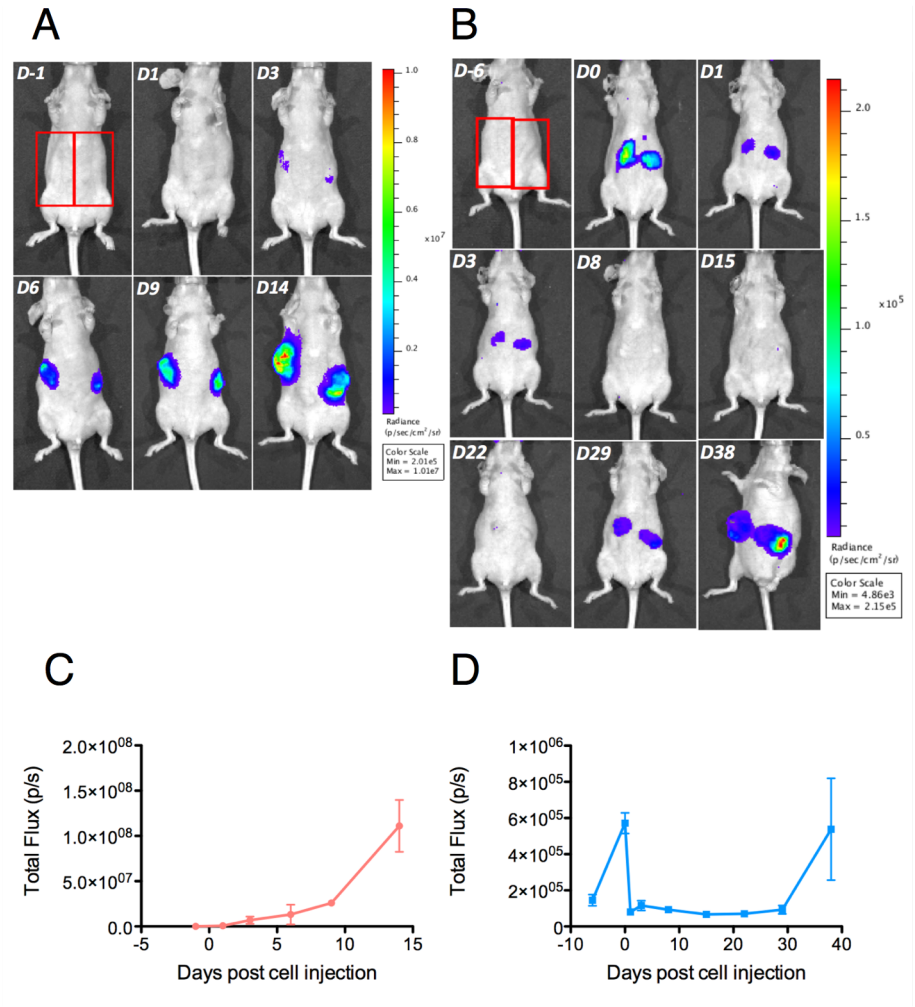
A
D-1
D1
D3
D6
D9
D14
1.0
0.8
0.6
0.4
0.2
x10^7
Radiance (p/sec/cm²/sr)
Color Scale
Min = 2.01e5
Max = 1.01e7
B
D-6
D0
D1
D3
D8
D15
D22
D29
D38
2.0
1.5
1.0
0.5
x10^5
Radiance (p/sec/cm²/sr)
Color Scale
Min = 4.86e3
Max = 2.15e5
C
Total Flux (p/s)
2.0×10^08
1.5×10^08
1.0×10^08
5.0×10^07
0.0
-5
0
5
10
15
Days post cell injection
D
Total Flux (p/s)
1×10^06
8×10^05
6×10^05
4×10^05
2×10^05
0
-10
0
10
20
30
40
Days post cell injection

Figure 3

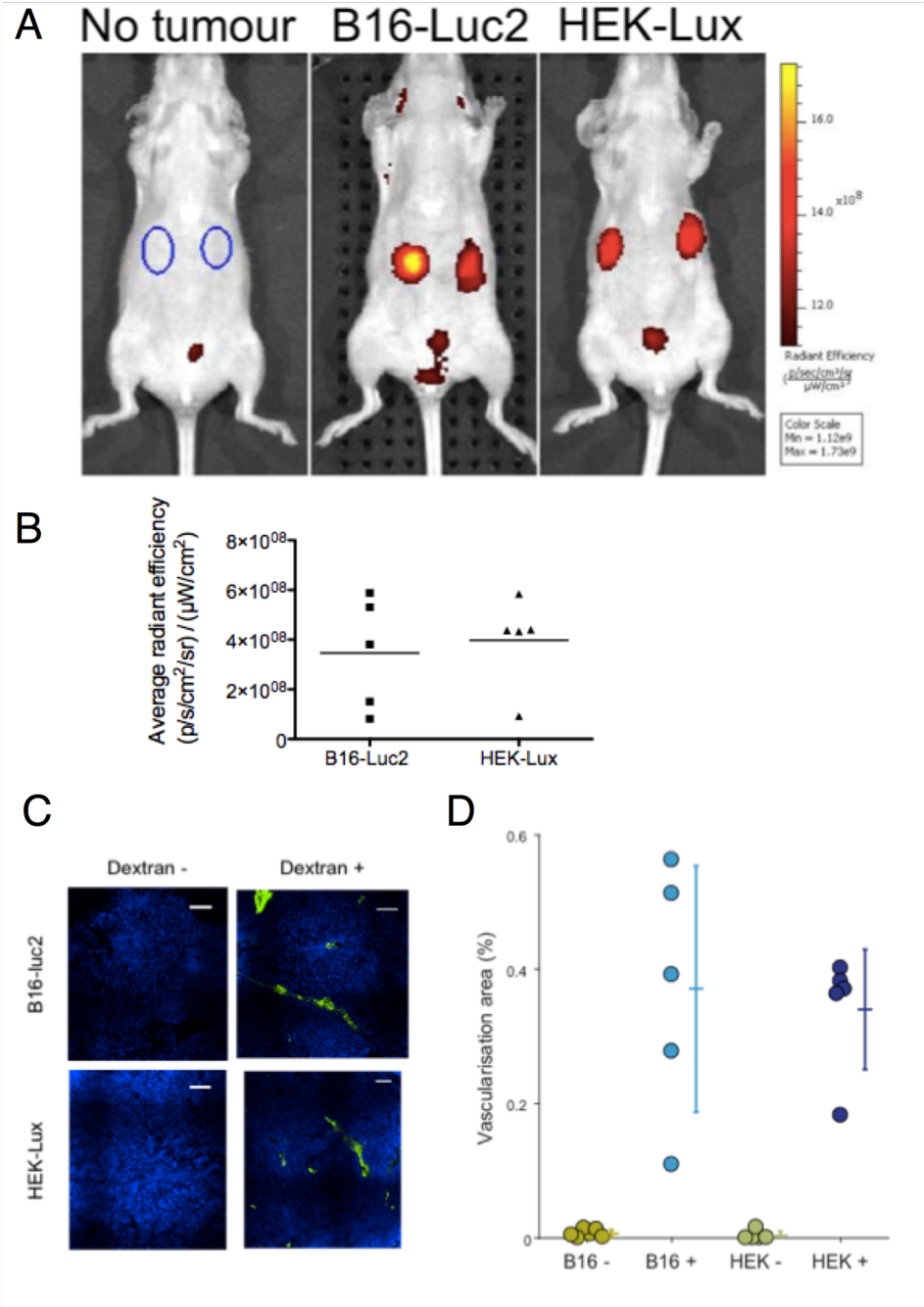
A
No tumour
B16-Luc2
HEK-Lux
16.0
14.0
x10^8
12.0
Radiant Efficiency
Color Scale
Min = 1.12e9
Max = 1.73e9
B
Average radiant efficiency
(p/s/cm²/sr) / (µW/cm²)
8×10^08
6×10^08
4×10^08
2×10^08
0
B16-Luc2
HEK-Lux
C
Dextran -
Dextran +
B16-luc2
HEK-Lux
D
Vascularisation area (%)
0.6
0.4
0.2
0
B16 -
B16 +
HEK -
HEK +

Figure 4

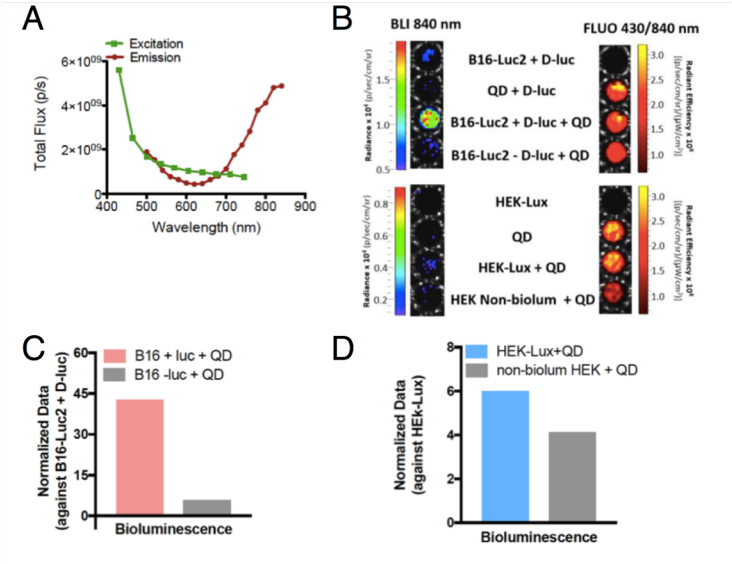
A
Excitation
Emission
Total Flux (p/s)
Wavelength (nm)
B
BLI 840 nm
FLUO 430/840 nm
B16-Luc2 + D-luc
QD + D-luc
B16-Luc2 + D-luc + QD
B16-Luc2 - D-luc + QD
HEK-Lux
QD
HEK-Lux + QD
HEK Non-biolum + QD
C
B16 + luc + QD
B16 -luc + QD
Normalized Data (against B16-Luc2 + D-luc)
Bioluminescence
D
HEK-Lux+QD
non-biolum HEK + QD
Normalized Data (against HEK-Lux)
Bioluminescence

Figure 5

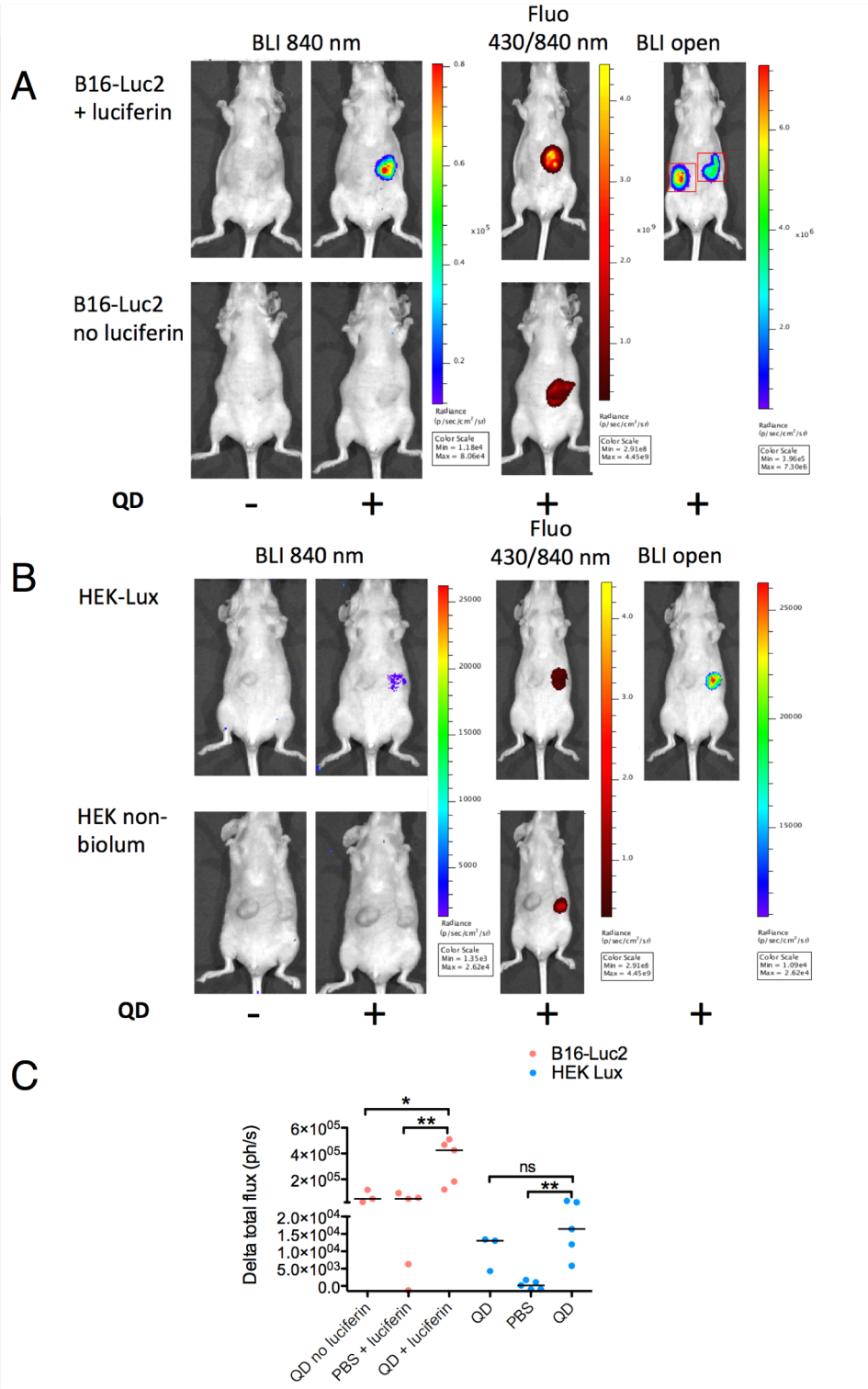
A
BLI 840 nm
Fluo
430/840 nm
BLI open
B16-Luc2
+ luciferin
B16-Luc2
no luciferin
QD
-
+
+
+
B
BLI 840 nm
Fluo
430/840 nm
BLI open
HEK-Lux
HEK non-
biolum
QD
-
+
+
+
C
B16-Luc2
HEK Lux
Delta total flux (ph/s)
6×10^05
4×10^05
2×10^05
2.0×10^04
1.5×10^04
1.0×10^04
5.0×10^03
0.0
*
**
ns
**
QD no luciferin
PBS + luciferin
QD + luciferin
QD
PBS
QD